Universal threshold and Arnold tongues in Kerr ring microresonators

D.V. Skryabin,* Z. Fan, A. Villois, and D.N. Puzyrev
Department of Physics, University of Bath, Bath BA2 7AY, UK

We report that an instability boundary of a single-mode state in Kerr ring microresonators with ultrahigh quality factors breaks the parameter space span by the pump laser power and frequency into a sequence of narrow in frequency and broad in power resonance domains - Arnold tongues. Arnold resonances are located between the Lugiato-Lefever (lower) and universal (higher) thresholds. Pump power estimates corresponding to the universal threshold are elaborated in details. RF-spectra generated within the tongues reveal a transition between the repetition-rate locked and unlocked regimes of the side-band generation.

Microresonators with Kerr nonlinearity continue to redefine fundamental and applied aspects of frequency conversion, comb generation, and dissipative optical solitons [1, 2]. Lugiato-Lefever equation (LLE), which is a key theoretical model in this area [3], has been originally proposed in the context of pattern formation in an optical resonator supporting a single longitudinal and many transverse modes and has gained broad interdisciplinary significance, see [4] and references thereafter. Some earlier works [5, 6] reported multi-mode instabilities in bistable cavities. Pattern formation is, of course, a vast contemporary research area [7, 8], that sprang from the famous paper by Alan Turing on instabilities of homogeneous states of morphogens [9]. Cell structures considered by Turing were taken circular for simplicity, which brings his approach remarkably close to the context of ring microresonators.

In this work, we present a detailed theory showing that in ring microresonators with ultrahigh quality factors there exists a second threshold, *universal threshold*, different from the one originally reported by Lugiato and Lefever [4], i.e., LL threshold. A primary parameter controlling the difference between the two thresholds is the finesse, or the degree of discreteness, of the residual spectrum (i.e., residual finesse) of the resonator modes left after the career frequency (200THz) and the resonator repetition rate (10-10^2GHz) have been subtracted. The non-equidistant inter-mode separations left to work with scale with the second order dispersion, i.e., belong to the medium-low-RF range ($<$ 10MHz). If the residual finesse is large enough, then the parameter space between the LL and universal thresholds is split into a sequence of narrow in frequency and wide in power instability domains - *Arnold tongues*. So that a single-mode state can be either stable or unstable above the LL threshold, and it becomes fully unstable only after the universal threshold has been crossed.

Arnold tongues are well known features of the parametrically driven [10] and coupled oscillator systems [11, 12], where they shape intervals of instabilities, frequency and phase locking. Periodicity embedded into model equations is an important property underpinning the formation of Arnold tongues. Various synchronisation phenomena have been reported in microring resonators, see, e.g., [13–15], while Ref. [16] made direct observations of the Arnold tongues due to repetition-rate locking between the soliton sequences in a two-ring system coupled by a fibre. Nonlinear effects in optics and fluid mechanics with periodic modulation of parameters have been attracting considerable recent attention, see, e.g., [17–19]. Our present work deals with a single-ring unidirectional LLE that does not include any time-periodic parameter variations, but is solved in a circular domain.

Amplitude ψ of the electric field in a ring microresonator can be expressed as a superposition of angular harmonics: $\psi = \sum_\mu \psi_\mu(t) e^{i\mu\vartheta}$. Here μ and ψ_μ are the mode numbers and amplitudes. ϑ is an angle varying along the ring, $\vartheta \in [0, 2\pi)$. Frequency of each resonance, ω_μ, is counted from the ω_0 reference and approximated as

$$\omega_\mu = \omega_0 + D_1\mu + \tfrac{1}{2}D_2\mu^2,\ \mu = 0, \pm1, \pm2, \dots. \qquad (1)$$

$D_1/2\pi$ is the repetition rate parameter, which is also the resonator free spectral range (FSR). D_2 is the second order dispersion, characterising how FSR is changing with μ. For example, a CaF_2 resonator in [20] has $D_1/2\pi$ = 15GHz, and $D_2/2\pi$ can be taken between $-$1kHz and +1kHz for $\omega_0/2\pi$ close to 200THz. If $\kappa/2\pi$ is the resonance linewidth, then the resonator finesse is

$$\mathcal{F}_\mu = \frac{\omega_{\mu\pm1} - \omega_\mu}{\kappa} = \mathcal{F} - \alpha_\mu,\ \mathcal{F} = \frac{D_1}{\kappa}, \qquad (2)$$

where we take +1 for $\mu > 0$ and -1 for $\mu < 0$. Here, $\mathcal{F}$ is the dispersion free finesse, and

$$\alpha_\mu = \mathcal{F} - \mathcal{F}_\mu = -\big(\mu \pm \tfrac{1}{2}\big)\mathcal{F}_d,\ \mathcal{F}_d = \frac{D_2}{\kappa}. \qquad (3)$$

α_μ is the residual finesse, and $\mathcal{F}_d$ is the finesse dispersion. $\mathcal{F}_d$ can be either positive (anomalous dispersion, $D_2 > 0$) or negative (normal dispersion, $D_2 < 0$). $Q = \omega_0/\kappa$ is the resonator quality factor. $Q = 3 \cdot 10^9$, which is a conservative number for CaF_2 resonators, gives $\kappa/2\pi$ = 67kHz, $\mathcal{F} = 22 \cdot 10^4$, and $|\mathcal{F}_d| \lesssim 1.5 \cdot 10^{-2}$ for these samples [20, 21]. For the ultrahigh $Q = 10^{11}$ samples [22], $\kappa/2\pi$ = 2kHz, $\mathcal{F} = 750 \cdot 10^4$, and $|\mathcal{F}_d| \lesssim 0.5$.

LLE derived from the Maxwell equations [23–25] is

$$i\partial_t\psi = \delta_0\psi - \tfrac{1}{2}D_2\partial_\theta^2\psi - i\tfrac{1}{2}\kappa\,(\psi-\mathcal{H}) - \gamma|\psi|^2\psi, \quad (4)$$

$$\delta_0 = \omega_0 - \omega_p, \quad (5)$$

where $\theta = \vartheta - D_1 t$, ω_p is the pump laser frequency and δ_0 is its detuning from the cavity resonance ω_0. $\mathcal{H}^2$ is the intracavity pump power. $\gamma/2\pi = 10\text{kHz/W}$ is the nonlinear parameter, with its value estimated for the CaF_2 resonators. Transformation to the rotating reference frame, $\vartheta \to \theta$, replaces the linear resonator spectrum having the finesse $\mathcal{F}_\mu$ with the spectrum of the linear part of the LL model having the residual finesse α_μ. For details of Eq. (4) derivation and γ definition, see Supplemental Material (SM) and Ref. [25].

Single mode solution, $\psi(t,\theta) = \psi_0$, of Eq. (4) is $\psi_0 = -i\frac{1}{2}\kappa\mathcal{H}(\delta_0 - \Omega - i\frac{1}{2}\kappa)^{-1}$, where $\Omega \equiv \gamma|\psi_0|^2 > 0$ solves the cubic equation,

$$\gamma\mathcal{H}^2 = \Omega + \Omega\,(\delta_0-\Omega)^2\,\frac{4}{\kappa^2},\ \mathcal{H}^2 = \frac{\eta}{\pi}\mathcal{F}\mathcal{W}. \quad (6)$$

$\mathcal{W}$ is the pump laser power, and $\eta = \kappa_c/\kappa < 1$ is the coupling efficiency between the pump and the ω_0 resonance. κ_c is the loss rate due to coupling. Ω measures power of the $\mu = 0$ mode, $|\psi_0|^2$, scaled to the frequency units. The system becomes bistable providing three positive solutions for Ω coexist, see SM Fig. 2.

To study frequency conversion, we perturb ψ_0 by a pair of side-band modes with momenta μ and relatively small powers [8],

$$\psi = |\psi_0|e^{i\phi_0} + \psi_\mu e^{\lambda_\mu t + i\mu\theta} + \psi^*_{-\mu}e^{\lambda^*_\mu t - i\mu\theta}, \quad (7)$$

where $\phi_0 = \arg\psi_0$. Linearisation of Eq. (4) gives $i\partial_t\vec{q}_\mu = \widehat{V}_\mu\vec{q}_\mu$, where $\vec{q}_\mu = (\psi_\mu, \psi_{-\mu})^T$, and

$$\widehat{V}_\mu = \begin{bmatrix} \Delta_\mu - 2\Omega - i\frac{1}{2}\kappa & -\Omega e^{i2\phi_0} \\ \Omega e^{-i2\phi_0} & -\Delta_\mu + 2\Omega - i\frac{1}{2}\kappa \end{bmatrix}, \quad (8)$$

$$\Delta_\mu = \delta_0 + \tfrac{1}{2}D_2\mu^2 \equiv \big(\omega_0 + \tfrac{1}{2}\kappa\mu^2\mathcal{F}_d\big) - \omega_p. \quad (9)$$

Δ_μ is the residual spectrum having the residual finesse, α_μ. With ω_p and $D_1\mu$ being subtracted, the residual spectrum represents the medium, $\sim 10\text{MHz}$, to the super-low end of the RF spectrum [26, 27].

Frequency $\Omega > 0$ belongs to the RF range. It is simultaneously responsible for the nonlinear shifts of the resonances and for the coupling between the $\pm\mu$ side-bands. Setting $\vec{q}_\mu \sim e^{\lambda_\mu t}$ gives an equation for λ_μ: $\lambda_\mu\big(\lambda_\mu + \kappa\big) = 3\big(\Omega^{(1)}_\mu - \Omega\big)\big(\Omega - \Omega^{(2)}_\mu\big)$, where

$$\Omega^{(1),(2)}_\mu = \tfrac{2}{3}\Delta_\mu \pm \tfrac{1}{3}\sqrt{\Delta^2_\mu - \tfrac{3}{4}\kappa^2}. \quad (10)$$

$\Omega^{(2)}_\mu < \Omega < \Omega^{(1)}_\mu$ sets an interval with the exponential growth of $\pm\mu$ side-bands, see SM Fig. 2. $\lambda_\mu = \lambda_{-\mu}$ and, hence, choosing $\mu > 0$ for $\mathcal{F}_d < 0$ and $\mu < 0$ for $\mathcal{F}_d > 0$, does not restrict the generality, while conveniently sets the residual finesse to $\alpha_\mu = |\mathcal{F}_d|\big(|\mu| + \frac{1}{2}\big) > 0$ used below.

For a multimode system one can define the threshold by extending the prime condition, $\lambda_\mu = 0$, with an axillary one $\partial_\mu\lambda_\mu = 0$. The latter is well known in pattern formation theory [7] and is routinely used in nonlinear optics to find threshold conditions for the most unstable modes [8]. In our case, this gives $\Omega = \Omega^{(i)}_\mu$, $\partial_\mu\Omega^{(i)}_\mu = 0$ with $i =$ either 1 or 2. $i = 2$ leads to,

$$\Delta_\mu = \kappa,\ \Omega^{(2)}_\mu = \tfrac{1}{2}\kappa. \quad (11)$$

$i = 1$ gives $\Omega^{(1)}_\mu = -\frac{1}{2}\kappa$, but $\Omega > 0$, and hence $\Omega = \Omega^{(1)}_\mu$ threshold never comes first as Ω is increased (for μ being fixed, see SM Fig. 2). However, it exists and plays a role in the frequency conversion scenarios described below.

$\Delta_\mu = \kappa$ and Eq. (9) define a discrete sequence of the pump laser frequencies

$$\omega_p^{(\mu L)} = \omega_0 + \tfrac{1}{2}\kappa\mu^2\mathcal{F}_d - \kappa, \quad (12)$$

along the threshold condition $\Omega = \Omega^{(2)}_\mu$. The corresponding intracavity power, $\mathcal{H}^2_{\mu L}$, required for generation of a mode μ is found substituting $\Omega \to \Omega^{(2)}_\mu = \kappa/2$ and $\delta_0 \to \delta_0^{(\mu L)} \equiv \omega_0 - \omega_p^{(\mu L)}$ into Eq. (6),

$$\gamma\mathcal{H}^2_{\mu L} = \tfrac{1}{2}\kappa\big[(\mu^2\mathcal{F}_d - 1)^2 + 1\big]. \quad (13)$$

Eqs. (12), (13) define explicitly a set of the pump laser frequencies and powers (in s^{-1} and Watts, respectively) defining a threshold for the frequency conversion via generation of the $\pm\mu$ pair of modes. Here and below the sub- and super-script L stands for the LL-threshold.

Solving Eq. (12) for μ^2 and using it in Eq. (13) redefines $\mathcal{H}^2_{\mu L}$ via $\delta_0^{(\mu L)}$,

$$\gamma\mathcal{H}^2_{\mu L} = \tfrac{1}{2}\kappa\big[\big(\tfrac{2}{\kappa}\delta_0^{(\mu L)} - 1\big)^2 + 1\big]. \quad (14)$$

If one assumes $\delta_0^{(\mu L)}$ to vary continuously, then Eq. (14) appears as a tilted parabola in the $(\mathcal{H}^2, \delta_0)$ bifurcation plane, see, e.g., [24] and the top panel in Fig. 1.

For us, it is however crucial that $\delta_0^{(\mu L)}$ represents a discrete set of values, $\mu \in \mathbb{Z}$, while the laser power and frequency still can be tuned continuously. Hence, the instability threshold in the power-frequency space also exists between the points specified by Eqs. (12), (13). In order to find it, one can substitute $\Omega = \Omega^{(1)}_\mu$ and $\Omega = \Omega^{(2)}_\mu$ directly to Eq. (6) and compute $\mathcal{H}^2$ vs δ_0 for every μ. The boundary found this way is shown in Fig. 1 for the moderate, high and ultrahigh$-Q$. As Q is increased from 10^9 to 10^{12}, the corresponding finesse dispersion, $\mathcal{F}_d$, increases from being $\sim 10^{-3}$ to ~ 1. One can see, that the true instability boundary wobbles above the LL-threshold, given by Eq. (14). Hence, the latter constitutes a lower limit for the former. In the

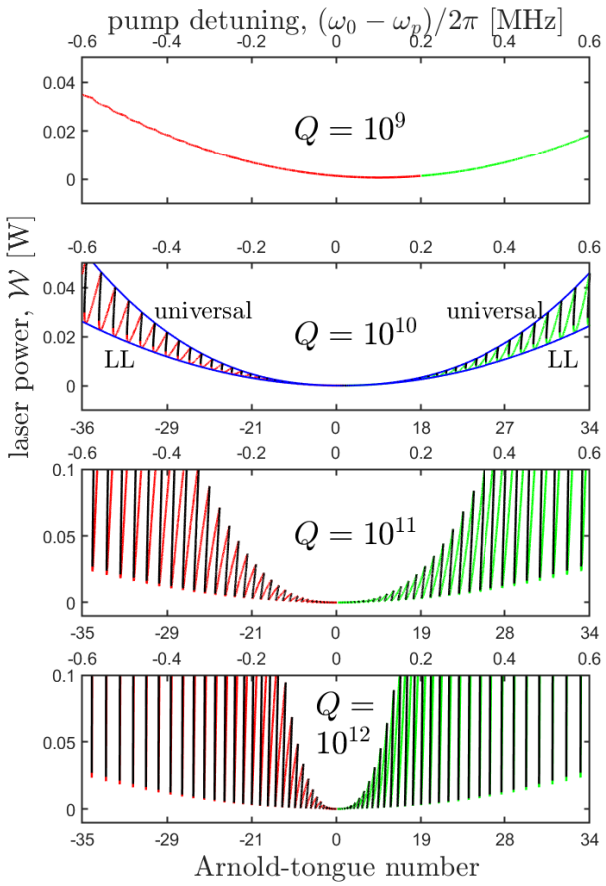

FIG. 1. Instability thresholds and Arnold tongues in the detuning-pump power, $(\delta_0, \mathcal{W})$, plane for varying quality factors, Q. $\delta_0 = \omega_0 - \omega_p$ is shown along the top horizontal axes, while the bottom ones show the corresponding resonance numbers μ for the $Q = 10^{10}$, 10^{11}, 10^{12} (i.e., $|\mathcal{F}_d| = 0.05, 0.5, 5$) cases. The $Q = 10^9$ panel with $|\mathcal{F}_d| = 0.005$ has no tongues. Anomalous dispersion ($\mathcal{F}_d > 0$) corresponds to the red and normal dispersion ($\mathcal{F}_d < 0$) to the green parts of the plots. The single mode state, ψ_0, is unstable above the red ($\Omega = \Omega_\mu^{(2)}$), green ($\Omega = \Omega_\mu^{(2)}$) and black ($\Omega = \Omega_\mu^{(1)}$) lines. $Q = 10^{10}$ panel shows the universal and LL thresholds with blue lines. Side-bands $\pm\mu$ are generated in pairs for a given δ_0, independently if the respective tongue number is positive or negative. $\eta = \kappa_c/\kappa = 0.5$ is hold fixed.

ultrahigh$-Q$ cases, deviations from the LL-threshold become very large, and the parameter space becomes broken into a sequence of narrow in frequency and wide in power resonance structures - *Arnold tongues*. One can also note that the condition $\Omega = \Omega_\mu^{(1)}$ (black lines) comes into play for higher Q's by shaping one of the two sides of the tongues. However, the very tips of the tongues and a small interval on the left of them are always given by $\Omega = \Omega_\mu^{(2)}$ (red and green lines) as per Eq. (14), see Fig.1, SM Figs. 3,5.

There is also a well defined boundary that limits the wobbling instability threshold from above, Fig. 1. We call this boundary line a *universal threshold*, i.e., a line above which the narrow intervals of stability between the Arnold tongues cease to exist. This happens via the power, i.e., nonlinearity, induced broadening of the tongues.

The universal threshold is made of the cusp points where the bifurcation lines, corresponding to the discretely changing μ's, intersect. As one can see, these intersections can and most often do involve the black, $\Omega = \Omega_\mu^{(1)}$, lines. Formally, locations of the cusps can be found applying

$$\Omega = \Omega_\mu^{(2)} = \Omega_{\mu\pm1}^{(i)}, i = 1, 2. \tag{15}$$

The above is a pair of the double, i.e., co-dimension-two [28], conditions that mark a sequence of the co-dimension-two bifurcation points happening across the orthogonal μ and $\mu \pm 1$ subspaces and forming the universal threshold line in the pump-power–pump-frequency parameter space, see Fig. 1.

Solving Eqs. (15) with $i =$ either 1 or 2 gives

$$\Delta_\mu = \kappa\big(\tfrac{1}{2}\alpha_\mu + \sqrt{1+\alpha_\mu^2}\,\big). \tag{16}$$

$\Omega_\mu^{(2)} = \Omega_{\mu\pm1}^{(2)}$ is satisfied for $\alpha_\mu < \alpha_{\mu_d}$, and it is replaced with $\Omega_\mu^{(2)} = \Omega_{\mu\pm1}^{(1)}$ for $\alpha_\mu > \alpha_{\mu_d}$, where

$$\alpha_{\mu_d} = \frac{1}{\sqrt{3}},\ \mu_d = \frac{1}{|\mathcal{F}_d|\sqrt{3}} - \frac{1}{2}, \mu_d \in \mathbb{R}. \tag{17}$$

Algebra leading to Eqs. (16), (17) is outlined in SM.

Pump frequencies at the cusps along the universal threshold are found from Eqs. (16) and (9),

$$\omega_p^{(\mu U)} = \omega_p^{(\mu L)} + \kappa\big(1 - \tfrac{1}{2}\alpha_\mu - \sqrt{1+\alpha_\mu^2}\,\big), \tag{18}$$

cf., Eq. (12).

The residual spectrum, see Eq. (9), is non-equidistant due to μ^2, and therefore even for very small $\mathcal{F}_d$'s there always be a sufficiently large μ making it discrete. The residual finesse, α_μ, fully accounts for this: $\alpha_\mu \ll 1$ and $\alpha_\mu \gg 1$ being the quasi-continuous and discrete limits. An approach equivalent to estimating α_μ is to compare μ with μ_d, since $|\mu/(\mu_d\sqrt{3})| \simeq |\mu\mathcal{F}_d| \simeq \alpha_\mu$. Therefore, $|\mu/\mu_d| \ll 1$ corresponds to the quasi-continuous and $|\mu/\mu_d| \gg 1$ to the discrete limits. Other words, if a resonator has $|\mu_d| \sim 1$ then the entire residual spectrum can be considered discrete, while for $|\mu_d| \gg 1$, it is quasi-continuous if $|\mu| < |\mu_d|$.

Laser powers corresponding to the universal threshold, $\mathcal{W}_{\mu U}$, are recovered by substituting Δ_μ from Eq. (16) to Eqs. (10) and $\omega_p^{(\mu U)}$ to Eq. (5), and then using the found Ω's and detunings in Eq. (6). As per the previous chapter, the discrete limit, $\alpha_\mu \gg 1$, corresponds to the relatively large mode numbers, $|\mu/\mu_d| \gg 1$, and hence to

the relatively large detunings, $\delta_0 \to \omega_0 - \omega_p^{(\mu U)}$. In this limit the power equation, Eq. (6), simplifies to

$$\gamma\mathcal{H}_{\mu U}^2 \simeq \Omega\delta_0^2\frac{4}{\kappa^2},\ \alpha_\mu \gg 1. \tag{19}$$

While in the quasi-continuous limit δ_0 remains relatively small, $\sim \kappa \sim \Omega$ (see below), and all the terms in the right-hand side of Eq. (6) are balanced.

The next step towards getting transparent analytical expressions for $\mathcal{W}_{\mu U}$ is to consider how Eq. (16) can be approximated for large and small α_μ. In the quasi-continuous limit, Eq. (16) is

$$\tfrac{1}{2}\alpha_\mu + \sqrt{1+\alpha_\mu^2} = 1 + \mathcal{O}\big(\alpha_\mu\big),\ \alpha_\mu \ll 1. \tag{20}$$

Hence $\Delta_\mu \simeq \kappa$ and $\Omega_\mu^{(2)} \simeq \frac{1}{2}\kappa$, see Eqs. (16), (10). Taking a slightly stricter condition $\alpha_\mu \ll |\mu|^{-1}$, gives $\omega_p^{(\mu L)} \simeq \omega_0 - \kappa$. Thus, Eq. (6) is well approximated with $\gamma\mathcal{H}_{\mu U}^2 \simeq \kappa$, which coincides with the respective approximation for $\gamma\mathcal{H}_{\mu L}^2$ obtained from Eq. (13),

$$\mathcal{W}_{\mu U} \simeq \mathcal{W}_{\mu L} \simeq \frac{\pi}{\eta\mathcal{F}}\frac{\kappa}{\gamma} = \frac{\pi\kappa^2}{\gamma D_1\eta},\ \alpha_\mu \ll |\mu|^{-1}. \tag{21}$$

Convergence of the two thresholds in the limit of the quasi-continuous residual spectrum is evident from the $Q = 10^9$, $|\mathcal{F}_d| = 0.005$ panel in Fig. 1.

If the residual finesse is large, then Eq. (16) is

$$\tfrac{1}{2}\alpha_\mu + \sqrt{1+\alpha_\mu^2} = \tfrac{3}{2}\alpha_\mu + \mathcal{O}\big(\alpha_\mu^{-1}\big),\ \alpha_\mu \gg 1, \tag{22}$$

while the instability boundary develops Arnold tongues between the diverging LL and universal thresholds, see Fig. 1. Now, $\Delta_\mu \simeq \frac{3}{2}\kappa\alpha_\mu$ and $\Omega_\mu^{(2)} \simeq \frac{1}{2}\kappa\alpha_\mu$. Since $\omega_p^{(\mu U)} \simeq \omega_0 + \frac{1}{2}\kappa\mu\alpha_\mu$, the detuning in Eq. (6) is replaced with $\delta_0 \simeq -\frac{1}{2}\kappa\mu\alpha_\mu$. Applying Eqs. (19), (6) gives the pump power at the universal threshold,

$$\mathcal{W}_{\mu U} \simeq \frac{\pi}{\eta\mathcal{F}}\frac{\kappa\mu^2}{2\gamma}\alpha_\mu^3 \simeq \frac{\pi D_2^2}{2\gamma D_1}\left(\frac{|\mu D_2|}{\eta\kappa}\right)\mu^4, \alpha_\mu \gg 1. \tag{23}$$

The respective limit of the LL threshold, see Eq. (13), is

$$\mathcal{W}_{\mu L} \simeq \frac{\pi}{\eta\mathcal{F}}\frac{\kappa\mu^2}{2\gamma}\alpha_\mu^2 \simeq \frac{\pi D_2^2}{2\gamma D_1}\left(\frac{1}{\eta}\right)\mu^4, \alpha_\mu \gg 1. \tag{24}$$

Comparing Eqs. (23) and (24), one can see that the factor making the difference between the universal and LL powers, and hence measuring the relative depth of the Arnold tongues, is exactly α_μ, i.e., the residual finesse. Different scaling of the two threshold powers with the total loss κ, as described by Eqs. (23), (24), is obvious from the $Q = 10^{11}$ and 10^{12} panels in Fig. 1, where η is kept fixed and $Q \sim \kappa^{-1}$ is varied independently.

Before concluding, we make an initial touch on the links between the Arnold-tongue physics and RF-photonics [26]. The instantaneous and time-averaged

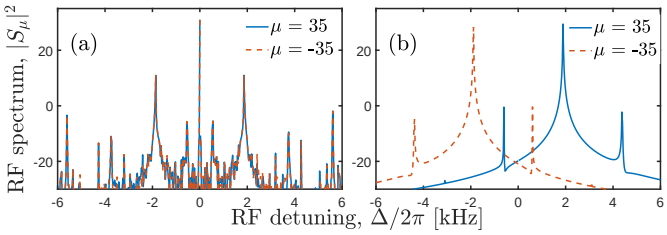

FIG. 2. RF spectra $|S_\mu(\Delta)|^2$ (in dBm) of the side-band amplitudes ψ_μ [29]. Blue lines correspond to $\mu = +35$ and the red dashed one – to $\mu = -35$. The spectra are calculated over 0.039s (597×10^6 loops). $D_2/2\pi = 1$kHz, $\gamma/2\pi = 10$kHz/W. (a) corresponds to the repetition-rate locking at $\mathcal{W} = 0.45$W, $\delta_0 = -0.5906$MHz. The blue and red lines overlap, and each of them is also symmetric relative to zero: $\langle\partial_t\phi_\mu\rangle = \langle\partial_t\phi_{-\mu}\rangle = 0$ [29]. (b) is the unlocked, i.e., frequency-domain symmetry breaking, regime at $\mathcal{W} = 0.4833$W, $\delta_0 = -0.5916$MHz. The blue/red lines have their spectral centres of mass for Δ positive/negative corresponding to $\langle\partial_t\phi_\mu\rangle = -\langle\partial_t\phi_{-\mu}\rangle = |\mu|d_{|\mu|} \simeq 2\pi \times 2$kHz.

mode frequencies are $\widetilde{\omega}_\mu(t) = \omega_p + D_1\mu + \partial_t\phi_\mu$ and $\langle\widetilde{\omega}_\mu\rangle = \omega_p + D_1\mu + \langle\partial_t\phi_\mu\rangle$. Here, the phase shift $\phi_\mu = -\arg\psi_\mu(t)$ is found solving Eq. (4), while $\omega_p + D_1\mu$ is recovered from how the envelope ψ is connected to the real electric field, see SM. Let's take the pump frequency and power tuned close to either the tongue tips ($\omega_p \simeq \omega_p^{(\mu L)}$, $\mathcal{W} \simeq \mathcal{W}_{\mu L}$) or to its edges ($\Omega = \Omega_\mu^{(i)}$), but away from the universal threshold, $\mathcal{W}_{\mu U}$, and away from the middle area of the tongue, see SM Figs. 3,5. Then, $\partial_t\phi_\mu$ emerge as either zeros or as periodic and weakly chaotic functions oscillating with relatively small amplitudes and giving $\langle\partial_t\phi_\mu\rangle = \langle\partial_t\phi_{-\mu}\rangle = 0$. The time-averaged repetition rate of the associated intra-cavity signals is generally defined as $(\langle\widetilde{\omega}_\mu\rangle - \langle\widetilde{\omega}_{-\mu}\rangle)/2|\mu|$. Hence, the repetition rates of the signals generated under these conditions are locked to D_1 either exactly or on average. This is the Adler-Arnold frequency locking [12], which in our case means the repetition-rate locking, since D_1 is set by ω_0 and does not depend on the pump parameters, ω_p and $\mathcal{W}$. In the coordinate space, the locked states correspond to the stationary or breathing Turing rolls rotating with the repetition rate of the linear resonator [30–37].

If ω_p is tuned towards the middle of the tongues and $\mathcal{W}$ is gradually increased, then the regimes with $\langle\partial_t\phi_\mu\rangle \neq \langle\partial_t\phi_{-\mu}\rangle$ are encountered. The averaged repetition rates are then $(\langle\widetilde{\omega}_\mu\rangle - \langle\widetilde{\omega}_{-\mu}\rangle)/2|\mu| = D_1 + d_{|\mu|}$. Here $d_{|\mu|} = (\langle\partial_t\phi_\mu\rangle - \langle\partial_t\phi_{-\mu}\rangle)/2|\mu|$ and it is a function of ω_p and $\mathcal{W}$, i.e., the repetition rate becomes unlocked. We found $d_{|\mu|}/2\pi$ to reach $\simeq 50$Hz, which is calculated from the RF offset of $\simeq 4$kHz between the modes $\mu = \pm 35$, see Fig. 2(b), and SM Fig. 4. Our stability analysis has the $\lambda_\mu = \lambda_{-\mu}$ symmetry, see Eqs. (10), (9). Thus, $\langle\partial_t\phi_\mu\rangle \neq \langle\partial_t\phi_{-\mu}\rangle$ implies the nonlinearity induced breaking of the $\mu \to -\mu$ symmetry in the frequency domain. Using the bifurcation theory terminology [28], this is a

pitchfork bifurcation, when a pair of the asymmetric solutions with $\pm|d_{|\mu|}|$ bifurcates from the symmetric $d_{|\mu|}=0$ state. In the coordinate space, these are the two families of the Turing rolls rotating with the $D_1 \pm |d_{|\mu|}|$ rates, see SM Fig. 4. $d_{|\mu|}=0$ implies that the RF spectra [29] of both side-bands are symmetric, while the $d_{|\mu|}\neq 0$ regimes have them asymmetric, cf. Figs. 2(a) and 2(b). Refs. [38–40] have reported the frequency-domain symmetry breaking of the counter-rotating waves in lasers and microresonators, while the case considered here deals with the co-propagating waves and is due to transition away from the Adler-Arnold frequency locking.

In summary: We derived the second instability threshold -*universal threshold*, and predicted the Arnold tongues in Kerr microresonators with ultrahigh quality factors. A sequence of Arnold resonances constitutes a fine, low-RF-scaled, spectral structure embedded inside the primary GHz-scaled resonator spectrum. Our results reveal a pathway linking the interdisciplinary Arnold-tongue concept with the development of the microresonator based light and RF sources [1, 2, 26].

This work was supported by the EU Horizon 2020 Framework Programme (812818, MICROCOMB).

* d.v.skryabin@bath.ac.uk

[1] A.L. Gaeta, M. Lipson, and T.J. Kippenberg, Photonic-chip-based frequency combs, Nat. Phot. **13**, 158 (2019).

[2] A. Pasquazi, M. Peccianti, L. Razzari, D. J. Moss, S. Coen, M. Erkintalo, Y. K. Chembo, T. Hansson, S. Wabnitz, P. Del'Haye, X. Xue, A. M. Weiner, and R. Morandotti, Micro-combs: A novel generation of optical sources, Phys. Rep. **729**, 1 (2018).

[3] T.J. Kippenberg, A.L. Gaeta, M. Lipson, and M. Gorodetsky, Dissipative Kerr solitons in optical microresonators, Science **361**, eaan8083 (2018).

[4] L. A. Lugiato and R. Lefever, Spatial Dissipative Structures in Passive Optical Systems, Phys. Rev. Lett. **58**, 2209 (1987).

[5] D. W. McLaughlin, J. V. Moloney, and A. C. Newell, New Class of Instabilities in Passive Optical Cavities, Phys. Rev. Lett. **54**, 681 (1985).

[6] L.A. Lugiato, and L.M. Narducci, Single-mode and multimode instabilities in lasers and related optical systems, Phys. Rev. A **32**, 1576-1587 (1985).

[7] M. Cross and H. Greenside, Pattern Formation and Dynamics in Nonequilibrium Systems (Cambridge University Press, 2009).

[8] L. Lugiato, F. Prati, and M. Brambilla, *Nonlinear Optical Systems* (Cambridge University Press, 2015).

[9] A.M. Turing, The chemical basis of morphogenesis, Proc. Royal Soc. B **237**, 37 (1952).

[10] V. I. Arnold, Remarks on the perturbation problem for problems of Mathieu type, Usp. Mat. Nauk, **38** 189203 (1983); Russ. Math. Surveys, **38**, 215233 (1983).

[11] V. I. Arnold, Small denominators and mappings of the circumference onto itself. Izv. Akad. Nauk Ser. Mat. **25**, 2186 (1961); AMS Transl. Ser. 2, **46**, 213284.

[12] A. Pikovsky, M. Rosenblum, and J. Kurths, Synchronization: A universal concept in nonlinear sciences (Cambridge University Press, 2001).

[13] Q.F. Yang, X. Yi, K.Y. Yang, and K. Vahala, Counter-propagating solitons in microresonators, Nat. Photon. **11**, 560 (2017).

[14] D. V. Skryabin and Y. V. Kartashov, Self-locking of the frequency comb repetition rate in microring resonators with higher order dispersions, Opt. Express **25**, 27442-27451 (2017).

[15] J.K. Jang, A. Klenner, X.C. Ji, Y. Okawachi, M. Lipson, and A.L. Gaeta, Synchronization of coupled optical microresonators, Nat. Photon. **12**, 688 (2018).

[16] J.K. Jang, X. Ji, C. Joshi, Y. Okawachi, M. Lipson, and A. L. Gaeta, Observation of Arnold Tongues in Coupled Soliton Kerr Frequency Combs, Phys. Rev. Lett. **123**, 153901 (2019).

[17] M. C. Cross and P. C. Hohenberg, Pattern formation outside of equilibrium, Rev. Mod. Phys. **65**, 851 (1993).

[18] F. Bessin, F. Copie, M. Conforti, A. Kudlinski, A. Mussot, and S. Trillo, Real-Time Characterization of Period-Doubling Dynamics in Uniform and Dispersion Oscillating Fiber Ring Cavities, Phys. Rev. X **9**, 041030 (2019).

[19] A. M. Perego, N. Tarasov, D. V. Churkin, S. K. Turitsyn, and K. Staliunas, Pattern Generation by Dissipative Parametric Instability, Phys. Rev. Lett. **116**, 028701 (2016).

[20] A. A. Savchenkov, A. B. Matsko, V. S. Ilchenko, I. Solomatine, D. Seidel, and L. Maleki, Tunable Optical Frequency Comb with a Crystalline Whispering Gallery Mode Resonator, Phys. Rev. Lett. **101**, 093902 (2008).

[21] I.S. Grudinin, N. Yu, and L. Maleki, Generation of optical frequency combs with a CaF_2 resonator, Opt. Lett. **34**, 878-880 (2009).

[22] A. A. Savchenkov, A. B. Matsko, V. S. Ilchenko, and L. Maleki, Optical resonators with ten million finesse, Opt. Express **15**, 6768-6773 (2007).

[23] T. Herr, V. Brasch, J.D. Jost, C.Y. Wang, N.M. Kondratiev, M.L. Gorodetsky, and T.J. Kippenberg, Temporal solitons in optical microresonators, Nat. Photon. **8**, 145-152 (2014).

[24] C. Godey, I.V. Balakireva, A. Coillet, and Y.K. Chembo, Stability analysis of the spatiotemporal Lugiato-Lefever model for Kerr optical frequency combs in the anomalous and normal dispersion regimes, Phys. Rev. A **89**, 063814 (2014).

[25] D.V. Skryabin, Hierarchy of coupled mode and envelope models for bi-directional microresonators with Kerr nonlinearity, OSA Continuum **3**, 1364-1375 (2020).

[26] J. Wu, X. Xu, T.G. Nguyen, S. T. Chu, B.E. Little, R. Morandotti, A. Mitchell, and D. J. Moss, RF Photonics: An optical microcombs' perspective, IEEE J. Sel. Top. Quant. Electr. **24**, 6101020 (2018).

[27] W. Weng, E. Lucas, G. Lihachev, V. E. Lobanov, H. Guo, M. L. Gorodetsky, and T. J. Kippenberg, Spectral Purification of Microwave Signals with Disciplined Dissipative Kerr Solitons, Phys. Rev. Lett. **122**, 013902 (2019).

[28] Y.A. Kuznetsov, *Elements of Applied Bifurcation Theory* (Springer, 2004).

[29] RF spectrum shown in Fig. 2 is defined as $S_\mu(\Delta) = \int \psi_\mu(t) e^{i\Delta t} dt$, where Δ is the RF detuning. The average low-RF frequency of ψ_μ ('low' since D_1 is subtracted) is $\int \Delta |S_\mu|^2 d\Delta / \int |S_\mu|^2 d\Delta = \langle \partial_t \phi_\mu \rangle$.

[30] G.K. Harkness, W.J. Firth, G.L. Oppo, and J.M. McSloy,

Computationally determined existence and stability of transverse structures. I. Periodic optical patterns, Phys. Rev. E **66**, 046605 (2002).

[31] V. Torres-Company, D. Castell-Lurbe, and E. Silvestre, Comparative analysis of spectral coherence in microresonator frequency combs, Opt. Express **22**, 4678-4691 (2014).

[32] W.H. Renninger, and P.T. Rakich, Closed-form solutions and scaling laws for Kerr frequency combs, Sci. Rep. **6**, 24742 (2016).

[33] Z. Qi, G. D'Aguanno, and C.R. Menyuk, Nonlinear frequency combs generated by cnoidal waves in microring resonators, J. Opt. Soc. Am. B **34**, 785-794 (2017).

[34] P. Parra-Rivas, D. Gomila, L. Gelens, and E. Knobloch, Bifurcation structure of periodic patterns in the Lugiato-Lefever equation with anomalous dispersion, Phys. Rev. E **98**, 042212 (2018).

[35] A. Coillet, Z. Qi, I.V. Balakireva, G. Lin, C.R. Menyuk and Y.K. Chembo, On the transition to secondary Kerr combs in whispering-gallery mode resonators, Opt. Lett. **44**, 3078 (2019).

[36] Z. Qi, S. Wang, J. Jaramillo-Villegas, M.H. Qi, A.M. Weiner, G. D'Aguanno, T.F. Carruthers, and C.R. Menyuk, Dissipative cnoidal waves (Turing rolls) and the soliton limit in microring resonators, Optica **6**, 1220-1232 (2019).

[37] S. Coulibaly, M. Taki, A. Bendahmane, G. Millot, B. Kibler, and M. G. Clerc, Turbulence-Induced Rogue Waves in Kerr Resonators, Phys. Rev. X **9**, 011054 (2019).

[38] D.V. Skryabin, A.G. Vladimirov, and A.M. Radin, Spontaneous phase symmetry-breaking due to cavity detuning in a class-A bidirectional ring laser, Opt. Commun. **116**, 109-115 (1995).

[39] D.V. Skryabin, Rotating and oscillating transverse patterns in an inhomogeneously broadened laser operating in a pair of doughnut modes, Quantum Semiclass. Opt. **8**, 485-493 (1996).

[40] W. Weng, R. Bouchand, E. Lucas, and T. J. Kippenberg, Polychromatic Cherenkov Radiation Induced Group Velocity Symmetry Breaking in Counterpropagating Dissipative Kerr Solitons, Phys. Rev. Lett. **123**, 253902 (2019).